

Supplementary Materials

I) FE model description:

An anatomically accurate model of knee joint consisting of the femur, tibial and patellar bones, articular surfaces, as well as the origins and insertions of the ligaments, was employed. This model was derived from digitized magnetic resonance image (MRI) transverse contours. The subject (a male of 28 years old with a height of 171 cm and weight of 79 kg) was placed in the transmit/receive circularly polarized knee coil of a Siemens Medical Systems Trio 3 Tesla for whole-body MRI. The Trio has a state-of-the-art 40mT/m gradient system with a slew rate of 200 T/m/s. A 3D FLASH sequence was used to obtain T1 weighted images with a spatial resolution of 5 x 5 x 1mm. The imaging plane was oriented along the anatomical transverse plane. These images are optimal to differentiate between the musculature, tendons, tissue fascia, and bone (Dhaher and Sun, 2006). The image data set was then imported into an MRI viewing and analysis package (Source Signal Imaging Inc., San Diego, CA) and re-sampled in the sagittal, coronal, and axial planes, providing convenient segmentation bases. The muscle-bone junctions were identified from the MRI images following the procedure outlined in (Dhaher and Kahn, 2002). Polygonal surfaces were used to generate a FE mesh of the knee joint using the Hypermesh (Altair Engineering, Troy, MI) pre-processor. Bones were modeled as rigid bodies (Donahue et al., 2002) using 4-node quadrilateral elements that shared linear elastic boundaries with the articular cartilages. Eight-node hexahedral elements were used to represent the articular cartilages, ligaments and menisci with an average size of 1.1 x 1.2 x 0.25 mm (Fig. 1). Element type and the total number of elements for each component of the knee joint are shown in table 1.

Table. 1: Mesh details of the knee joint.

<i>Set</i>	<i>Number of elements</i>	<i>Types of elements</i>
<i>Femoral cartilage</i>	15692	C3D8R
<i>Tibial cartilage</i>	11507	C3D8R
<i>Patellar cartilage</i>	5824	C3D8R
<i>Meniscus</i>	14880	C3D8R
<i>ACL</i>	3312	C3D8R
<i>PCL</i>	2224	C3D8R
<i>LCL</i>	1548	C3D8R

<i>MCL</i>	4076	C3D8R
<i>MPFL</i>	1160	C3D8R
<i>LPFL</i>	1008	C3D8R
<i>PT</i>	4100	C3D8R
<i>Graft</i>	31616	C3D8R
<i>QT</i>	2117	C3D8R
<i>Bones (femur, tibia and Patella)</i>	29906	S4R, S3R
<i>Total</i>	128943	C3D8R, S4R, S3R

This mesh size was obtained through a mesh sensitivity analysis, where a maximum of 6% difference in the von-Mises stress and principle strain was considered.

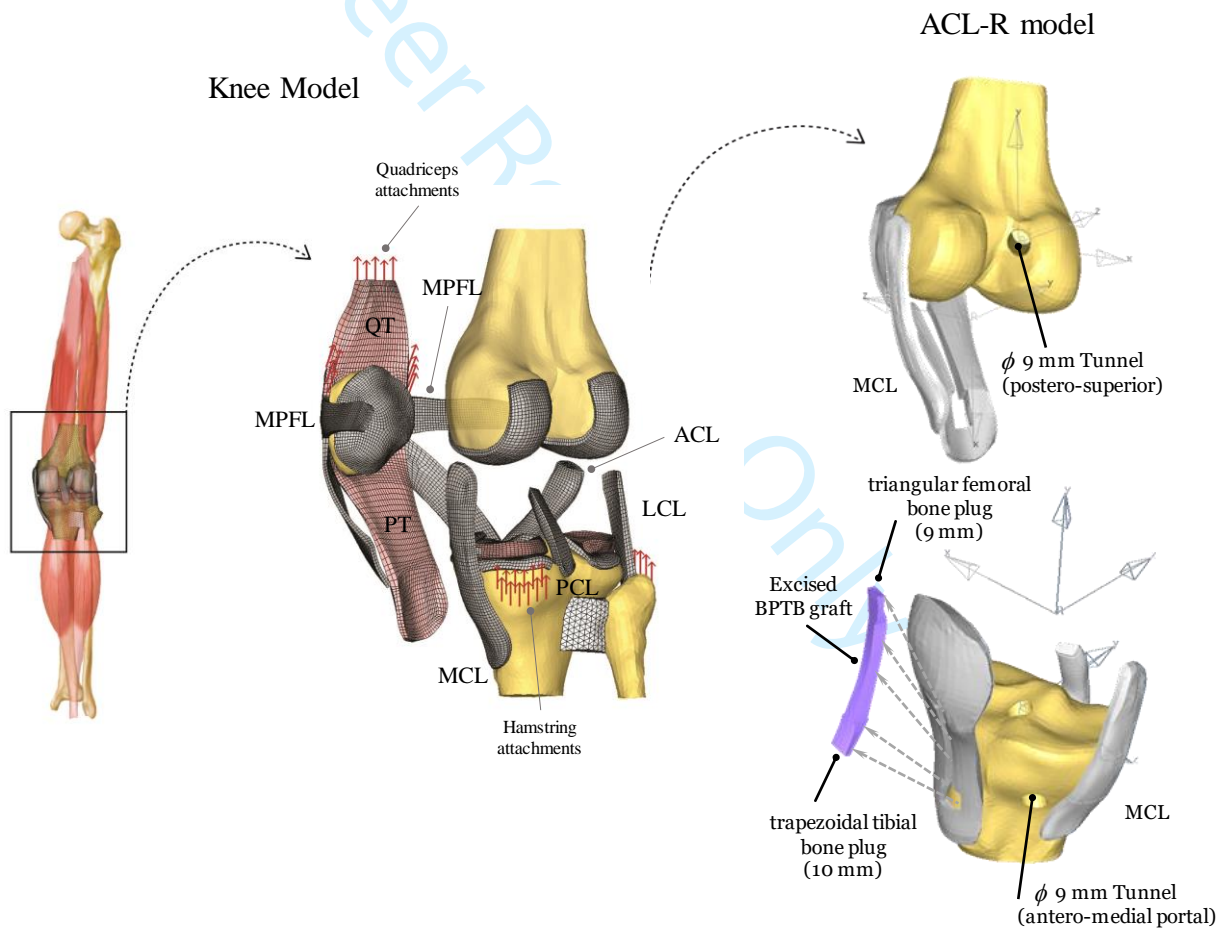


Figure. 1: Posterior view (left) of the bones and musculature of the right leg, showing the finite element model representing the knee joint. The middle one is an exploded posteromedial view of the knee FE model depicting the mesh used for the soft tissues and the locations of attachments for the quadriceps and hamstring muscles. The FE model consisted of four bones (femur, fibula, tibia, and patella) and continuum-based soft tissue structures. All relevant ligaments (anterior and posterior cruciate – ACL, PCL; medial and lateral collateral – MCL, LCL; medial and lateral patellofemoral – MPFL, LPFL; patellar tendon – PT; quadriceps tendon – QT), articular cartilage (femur, tibia, and patella), and menisci were included. The retinaculum ligaments were removed from the model due to the lack of experimental data. More details on the system of axes and the joint center calculations can be found in prior work (Schroeder, 2010, 2014). Key geometrical aspects of the ACL-R model with a description of tunnel dimension and locations are shown at right.

II) Description of parametric surgical simulations:

The ACL-R models were designed to be parametric with respect to the femoral tunnel sagittal and coronal angles (Fig. 2), quadrant coordinates of femoral tunnel placement (Fig. 3), the joint angle at which the BPTB graft is tensioned and fixed to the femoral tunnel (fixation angle), and the amount of the graft tensioning force (Fig. 4).

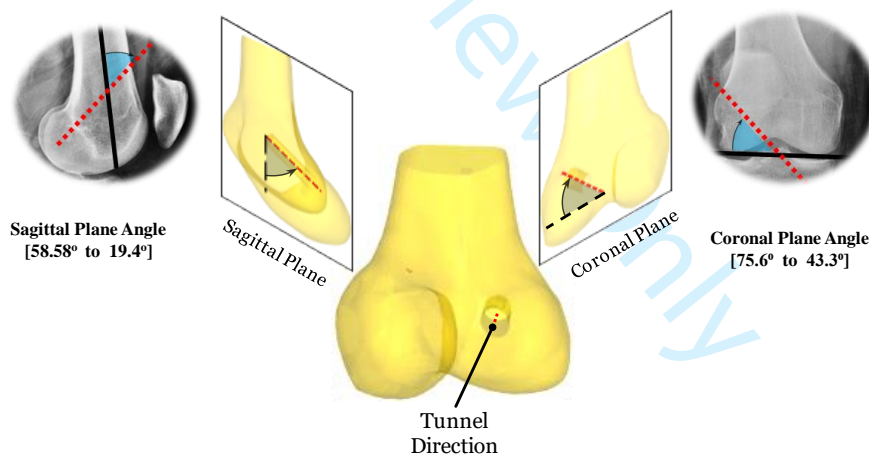


Figure 2: Femoral tunnel sagittal (A) and coronal angles (B). The sagittal and coronal angles were derived from Takeda et al., (2013).

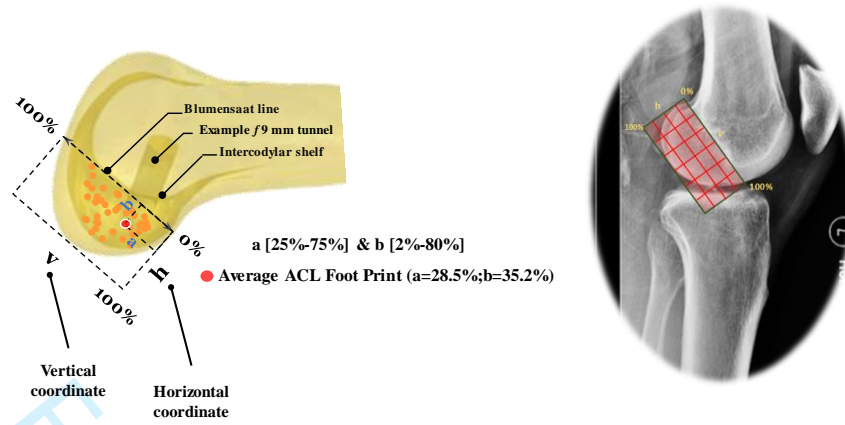


Figure 3: The tunnel placement constructed in the current model followed the quadrant method presented by Bernard et al. (1997). In the figure, v represents the line parallel to the Blumensaat line, and h represents the line perpendicular to the Blumensaat line. The position of the center of the femoral tunnel was defined by a , which represents the percentage distance from the most posterior contour in reference to the total length of the lateral condyle (v), and b , which represents the percentage distance from the intercondylar shelf (Blumensaat line) with respect to the total depth of the intercondylar notch (h). The average anatomic ACL location (footprint) is shown as reported by Piefer et al. (2012).

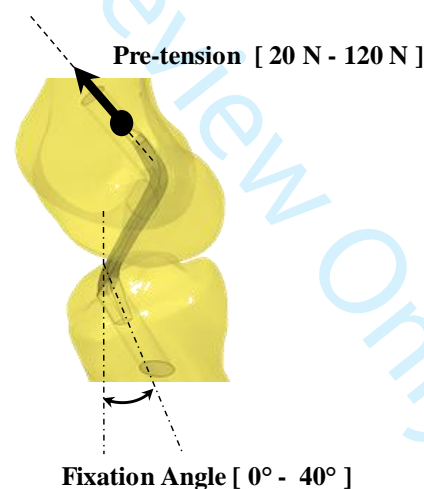


Figure 4: Fixation angle and graft pre-tensioning force. The ranges used for the graft pre-tensioning force and fixation angle were chosen based on anecdotal clinical evidence reported in several studies (Arnold and Netter, 1998; Nicholas, 2004; van Kampen, 1998; Yasuda et al., 1997; Yoshiya et al., 2002).

III) Details on ligament model:

The behavior of connective tissues was derived from an uncoupled representation of the strain

energy function defined as follows (Limbert and Middleton, 2004):

$$\psi_t(\bar{I}_1, \bar{I}_4, \bar{J}) = \psi_{nf}(\bar{I}_1) + \psi_f(\bar{I}_4) + \psi_{vol}(\bar{J}) \quad (1)$$

Where:

$$\begin{cases} \psi_{nf}(\bar{I}_1) = c_1(\bar{I}_1 - 3) \\ \psi_f(\bar{I}_4) = \frac{c_2}{2c_3} \exp(c_3(\bar{I}_4 - 1)^2) \quad \text{if } \bar{I}_4 > 1 \\ \psi_{vol}(\bar{J}) = \frac{1}{D}(\bar{J} - 1)^2 \end{cases} \quad (2)$$

where $(\psi_{nf}(\bar{I}_1) + \psi_f(\bar{I}_4))$, $\psi_{vol}(\bar{J})$ are the isotropic (f fibrillar and nf nonfibrillar) and volumetric parts, respectively. Next, the total stress can be computed from the equation:

$$\sigma_t = \frac{2}{J} F \left(\frac{\partial \psi_t}{\partial C} \right) F^T \quad (3)$$

where c_1 , c_2 and c_3 are the material parameters, $\bar{I}_1 = \text{tr}(\bar{C})$, $\bar{I}_4 = \bar{C} : (n_0 \otimes n_0)$ (n_0 is a unit vector specifying the fiber direction in the reference configuration), $\bar{C} = \bar{F}^T \bar{F}$ is the modified right Cauchy-Green tensor, $F = J^{2/3} \bar{F}$ is the deformation gradient tensor, $J = \det(F)$, and $\lambda_f = \sqrt{\bar{I}_4}$ (λ_f is the fiber stretch). The incompressibility penalty function is $(J - 1)^2$ and D is chosen to be 0.001 to simulate the near incompressibility of ligaments. Finally, this model was incorporated into the ligaments using Vumat-Abaqus (Quasi-static Analysis with Abaqus/Explicit).

Table 2: Material coefficients

Summary of the material coefficients of the ligament model.

	C₁ (fixed for each ligament)	C₂ Mean	C₃
MCL	1.0	35	$C_3 = 0.4 C_2$
LCL	1.0	35	$C_3 = 0.4 C_2$
ACL	0.5	2.0	$C_3 = 2.4 C_2 + 7.6$
PCL	0.2	1.2	$C_3 = 15.7 C_2 - 4.7$
MPFL	1.0	17.5	$C_3 = 0.4 C_2$
LPFL	1.0	17.5	$C_3 = 0.4 C_2$

The initial stretches (*in-situ* strains) were included in the FE model of the ligaments by defining three different configurations (Weiss et al., 1995): the stress-free (F_0) state, the reference state (F_r), and the current state F (Fig. 5).

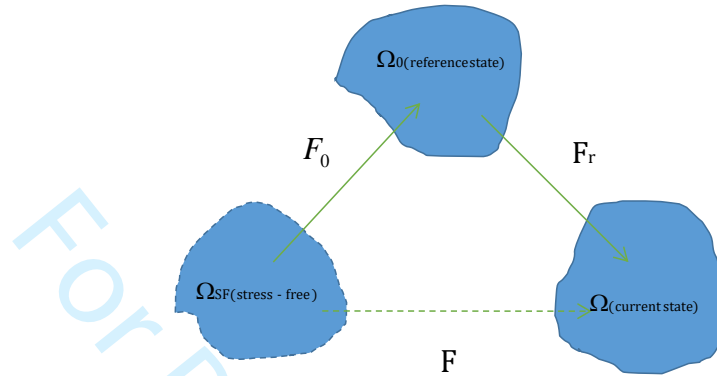


Figure 5: Multiplicative decomposition of the deformation gradient of the ligament.

Using a multiplicative decomposition, $F = F_0 F_r$, if an initial stretch field is assumed to be a uniaxial stretch, F_0 will take this form:

$$F_0 = \begin{bmatrix} \lambda_0 & 0 & 0 \\ 0 & \frac{1}{\sqrt{\lambda_0}} & 0 \\ 0 & 0 & \frac{1}{\sqrt{\lambda_0}} \end{bmatrix} \quad (4)$$

where λ_0 is the stretch along the local fiber-direction. The total stress corresponding to the current state can be computed from equation (3). The initial stretches in the PCL were set to zero at full extension (Peña et al. 2006), and for the rest of the ligaments, the initial stretches data from the experiments were enforced in discrete regions in search of static equilibrium in the finite element code (Dhaher et al., 2010).

IV) Details on multiscale cartilage model:

1) Microfibril:

The first step in the formulation is to leverage the multiplicative decomposition of the deformation gradient to describe the interplay between the shear and uniaxial deformation (Asaro and Rice, 1977; Lee, 1969). In that construct, the total deformation gradient tensor $\bar{F} = \bar{F}_s \bar{F}_f$, where s and f stand for shear and uniaxial deformation. We assume that the plastic flow associates only with the uniaxial deformation along

the fibril direction. The total deformation gradient tensor of fibril is expressed as $\bar{F}_f = \bar{F}_{fe}\bar{F}_{fp}$, where e and p stand for elastic and plastic. Combining the two multiplicative decompositions, the total deformation gradient tensor takes the form: $\bar{F} = \bar{F}_s \bar{F}_{fe} \bar{F}_{fp} = \bar{F}_e \bar{F}_p$ where, $\bar{F}_e = \bar{F}_s \bar{F}_{fe}$ (Fig .6):

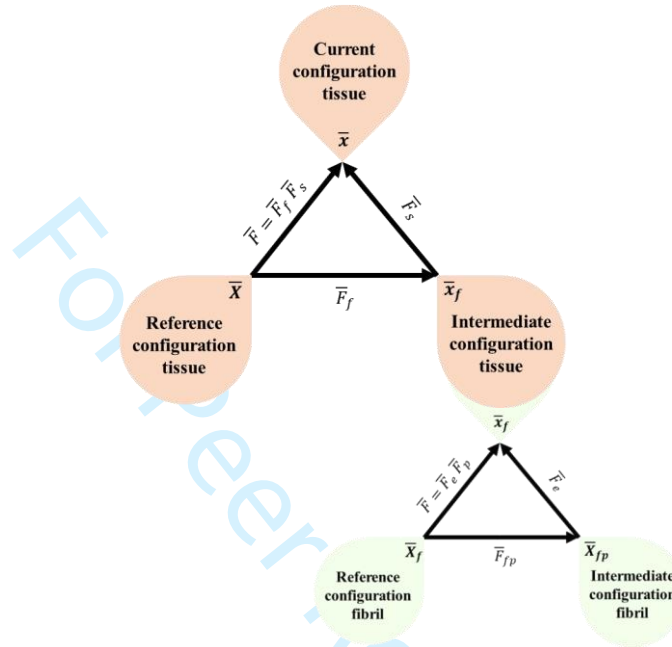


Figure 6: Multiplicative decomposition of the macroscopic deformation gradient of the cartilage.

At the microfibril level, the general expression of the strain energy function takes the following form:

$$\psi_{fl}(\bar{I}_{1e}, \bar{I}_{4e}) = \frac{1}{2} \mu^{fl}(\bar{I}_{4e})(\bar{I}_{1e} - 3) \quad (1)$$

where the shear moduli μ^{fl} is considered as a function of the elastic microfibril deformation with

$$\mu^{fl}(\bar{I}_{4e}) = \mu_0 \left(\tanh \left(a_1 (\bar{I}_{4e} - 1) \right) - a_2 \exp \left(a_3 (\bar{I}_{4e} - I_0) \right) \right) \quad (2)$$

The hyperbolic form of the strain energy function is advantageous in fitting the stiffness evolution of the microfibril predicted by molecular dynamic simulation (Buehler, 2006, 2008; Tang et al., 2009a; Tang et al., 2010). The strain energy function is then used to connect the effective stress (σ_{eff}) of the microfibril to the yield condition (i), the plastic strain rate ($\dot{\gamma}$) (ii) and the flow resistance ($g(t)$) (iii) of the tissue as follow:

$$\begin{cases} \sigma_{eff} = \frac{4}{3} \bar{I}_{4e} \frac{\partial \psi_{fl}}{\partial \bar{I}_{4e}} = g_0 = g_i + c\beta^2 & (i) \\ \dot{\gamma} = \dot{\gamma}_0 \left| \frac{\sigma_{eff}}{g(t)} \right|^{1/m} \text{sig}(\sigma_{eff}) & (ii) \\ g(t) = \int h \dot{\gamma} f(g) & (iii) \end{cases} \quad (3)$$

Where $f(g) = (1 - \frac{g(t)}{g_s})$, here $g_0 = g_i + c\beta^2$ represent the yield strength of the microfibril, which is a function of the crosslink density between tropocollagen molecules (TC M) ($g_i = 400 \text{ Mpa}$ and $c = 11$) (Tang et al., 2009a). After that, the plastic velocity gradient of the fibrils takes the deviatoric (*dev*) as follows:

$$\dot{F}_p F_p^{-1} = \dot{\gamma} \text{dev}(n_0 \otimes n_0) \quad (4)$$

This form was numerically integrated to compute the uniaxial plastic deformation gradient (\bar{F}_p) and then the uniaxial elastic deformation gradient (\bar{F}_e).

2) Fibril:

The collagen fibril was modeled as microfibril reinforced composite material with incompressible Neo-Hookean matrix, and the elastic strain energy of the fibril under extension ($\psi_{f_{bt}}$) and shear (ψ_{f_s}) are given by

$$\begin{cases} \psi_{f_{bt}}(\bar{I}_4, \bar{I}_{4e}) = v_{fl} \psi_{fl}(\bar{I}_{1ef}, \bar{I}_{4e}) + v_{ml} \left(\frac{\mu_{fm}}{2} (\bar{I}_{1f} - 3) \right) \\ \psi_{f_s}(\bar{I}_{1f}, \bar{I}_4, \bar{I}_{4e}) = \frac{1}{2} \mu^{efffb}(\bar{I}_{4e}) (\bar{I}_{1fb} - \bar{I}_{1f}) \\ \mu^{efffb}(\bar{I}_{4e}) = \mu_{fm} \frac{(1+v_{fl})\mu^{fl}(\bar{I}_{4e}) + \mu_0(1-v_{fl})}{(1-v_{fl})\mu^{fl}(\bar{I}_{4e}) + \mu_0(1+v_{fl})} \end{cases} \quad (5)$$

The total elastic strain energy density of the fibril (ψ_{fb}) is therefore written as

$$\psi_{fb}(\bar{I}_{1f}, \bar{I}_4, \bar{I}_{4e}) = \psi_{f_{bt}}(\bar{I}_4, \bar{I}_{4e}) + \psi_{f_s}(\bar{I}_{1f}, \bar{I}_4, \bar{I}_{4e}) \quad (6)$$

3) Cartilage :

The former process is used to treat the cartilage as fibril reinforced composite material characterized by axial (ψ_{tt}) and shear (ψ_{ts}) strain energy as follow

$$\begin{cases} \psi_{tt}(\bar{I}_1, \bar{I}_{1f}, \bar{I}_4, \bar{I}_{4e}) = v_f \psi_{fb}(\bar{I}_{1f}, \bar{I}_4, \bar{I}_{4e}) + v_m \left(\frac{\mu_m}{2} (\bar{I}_1 - 3) \right) \\ \psi_{ts}(\bar{I}_{1f}, \bar{I}_4, \bar{I}_{4e}) = \frac{1}{2} \mu^{eff}(\bar{I}_{4e}) (\bar{I}_1 - \bar{I}_{1f}) \\ \mu^{eff}(\bar{I}_{4e}) = \mu_m \frac{(1+v_f)\mu^{efffb}(\bar{I}_{4e}) + \mu_m(1-v_f)}{(1-v_f)\mu^{efffb}(\bar{I}_{4e}) + \mu_m(1+v_f)} \end{cases} \quad (7)$$

The total strain energy of tissue (ψ_t) is defined by

$$\psi_t(\bar{I}_{1f}, \bar{I}_4, \bar{I}_{4e}) = \psi_{tt}(\bar{I}_4, \bar{I}_{4e}) + \psi_{ts}(\bar{I}_{1f}, \bar{I}_4, \bar{I}_{4e}) + \psi_{vol}(\bar{J}) \quad (8)$$

We can further write the strain-energy function of the tissue as:

$$\begin{aligned} \psi_t = & \frac{1}{2}(v_f v_{ml} \mu_{fm} + v_m \mu_m) \left(\bar{I}_4 + \frac{2}{\sqrt{\bar{I}_4}} - 3 \right) + \frac{1}{2}(v_f v_{fl} \mu_{fl}) \left(\bar{I}_{4e} + \frac{2}{\sqrt{\bar{I}_{4e}}} - 3 \right) + \frac{1}{2} \mu^{eff} (\bar{I}_1 - \bar{I}_1(F_f)) \\ & + \frac{E_K}{2} (\bar{J} - 1)^2 \end{aligned} \quad (9)$$

4) Total stress :

By satisfying both the Clausius-Duhem dissipation inequality at the macroscopic continuum level and the constraint of the incompressibility of soft tissue, the total stress σ^t can be expressed with fibrillar σ^f and nonfibrillar σ^{nf} stress tensors as follow:

$$\begin{cases} \sigma^t = \sigma^{nf} + \sum \sigma_i^f \\ \sigma^{nf} = \frac{2}{J} \left(\bar{I}_1 \frac{\partial \psi_t}{\partial \bar{I}_1} dev(\bar{B}) + (E_K \bar{J} (\bar{J} - 1)) I \right) \\ \sigma_i^f = \left\{ \frac{2}{J} \left(\bar{I}_4 \frac{\partial \psi_t}{\partial \bar{I}_4} dev(n \otimes n) + \bar{I}_{4e} \frac{\partial \psi_t}{\partial \bar{I}_{4e}} dev(n_e \otimes n_e) \right) \right\}_i & \text{if } \bar{I}_{4i} > 1 \\ \sigma_i^f = 0 & \text{if } \bar{I}_{4i} \leq 1 \end{cases} \quad (10)$$

where i represent the number of the considered fibril by integration point. For more details on the construction of the constitutive model, please refer to the work of (Adouni and Dhaher, 2016; Adouni et al., 2019; Faisal et al., 2019; Tang et al., 2009b). This model was implemented with a Vumat-Abaqus (Quasi-static Analysis with Abaqus/Explicit). In the superficial zone of cartilage, the collagen fibrils are oriented horizontally, parallel to the medial and lateral directions. In the transitional zone of the cartilage, fibrils are randomly oriented (i.e., no dominant orientations) following a gradual curvature starting parallel from the superficial zone and turning perpendicular to the surface (along with the medial and lateral directions). In the deep zone, vertical fibrils are initially oriented perpendicular to the subchondral junction (Bi et al., 2006). Finally, all calibrated materials parameters, multiplicative decomposition, and invariant are listed in the tables below.

Table 3: Model parameters.

Materials parameters

μ_m	Shear Modulus of the Solid matrix
---------	-----------------------------------

E_K	Bulk modulus of the cartilage
v_f	volume fraction of the fibril
$n_{0(1,2,3)}$	fibril direction in the reference configuration
$n_{(1,2,3)}$	fibril direction in the deformed configuration
$n_{e(1,2,3)}$	fibril direction in the deformed configuration associated with the elasto-plastic flow
μ^{efffb}	The effective shear modulus involves the effects of shear interactions at the interface of the microfibril and fibril matrix.
μ^{eff}	The effective shear modulus involves the effects of shear interactions at the interface of the fibril and tissue matrix.
μ_{fm}	Shear modulus of the fibril matrix
μ_0	Shear modulus of the microfibril
v_{fl}	Volume fraction of the microfibril
I_0	Secondary stiffening of the microfibril
$a_{i(1,2,3)}$	Dimensionless microfibril parameters
g_0	Yield strength of microfibril
$\dot{\gamma}_0$	Initial plastic strain rate
$\dot{\gamma}$	Initial plastic strain rate
m	Rate Sensitivity
h	Hardening rate
Multiplicative decomposition and invariant	
$\bar{F} = \bar{F}_e \bar{F}_f^p$	Multiplicative decomposition of the deformation gradient into elastic and plastic parts
$\bar{I}_1 = \text{tr}(\bar{F} \bar{F}^T)$	First invariant
$\bar{I}_{1e} = \text{tr}(\bar{F}_e \bar{F}_e^T)$	First elastic invariant
$\bar{I}_4 = n_0^t \bar{B} n_0$	Invariant related to the fibril stretch
$\bar{I}_{4e} = n_0^t \bar{B}_e n_0$	Invariant related to the elastic fibril stretch
$\bar{I}_{1f} = \bar{I}_4 + 2\bar{I}_4^{-1/2}$	First invariant of fibril
$\lambda_f = \sqrt{\bar{I}_4}$	fibril principal stretch

Table 4: The statistically and manually calibrated material parameters of the articulate cartilage model.

Materials parameters		Lower bound	Upper bound	Calibrated distribution
μ_{fm}	Shear modulus of the fibril matrix (MPa)	0	4	2.879 (1.036)
μ_m	Shear modulus of the solid matrix (MPa)	NA	NA	0.1 to 0.4
μ_0	Shear modulus of the microfibril (MPa)	1000	4000	2906.928 (510.65)
ν_f	volume fraction of the fibril	NA	NA	0.15 to 0.18
ν_{fl}	Volume fraction of the microfibril	0.1	0.4	0.212 (0.034)
I_0	Secondary stiffening of the microfibril	1.6	2.8	2.118 (0.196)
a_1	Dimensionless microfibril parameter 1	0.1	2	1.163 (0.383)
a_2	Dimensionless microfibril parameter 2	100	1000	524.584 (195.205)
a_3	Dimensionless microfibril parameter 3	10	100	51.52 (18.024)
m	Rate Sensitivity	NA	NA	0.05
$\dot{\gamma}_0$	Initial plastic strain rate (1/s)	NA	NA	0.01
E_K	Bulk modulus of the cartilage	NA	NA	1/0.001
β	crosslink density between the TC M	NA	NA	9

NA: not applicable.

V) Details on the meniscus model:

Due to well-documented observations of the transverse and axial planes' isotropy in the meniscus, a special subclass of orthotropy - transverse isotropy was used to model the mechanical behavior of the meniscus (Fithian et al., 1990; Proctor et al., 1989; Tissakht and Ahmed, 1995). Axial, transverse, and circumferential axes characterize the meniscus's local coordinate system, assuming the transverse-axial plane as a plane of isotropy (Fig. 7). This assumption leads to a number of independent constants to be 5 in the matrix. Hence, the transverse isotropy is maintained considering circumferential modulus (E_C), transverse and axial modulus (E_t , E_a , such that $E_t = E_a$), Poisson's ratio (ν_{ct} , ν_{ca} , and $\nu_{ct} = \nu_{ca}$) that is defined as the ratio of the contractile strain in the transverse plane to the tensile strain in the circumferential direction under the load in the circumferential direction, Poisson's ratio, ν_{ta} , within the transverse plane, shear modulus, $G_t = G_a$, in the plane along the fiber direction. The stress-strain relationship for the transversely isotropic materials is defined as follows:

$$\begin{Bmatrix} \varepsilon_{11} \\ \varepsilon_{22} \\ \varepsilon_{33} \\ \gamma_{12} \\ \gamma_{13} \\ \gamma_{23} \end{Bmatrix} = \begin{bmatrix} 1/Et & -\vartheta ta/Et & -\vartheta ct/Ec & 0 & 0 & 0 \\ -\vartheta ta/Et & 1/Et & -\vartheta ct/Ec & 0 & 0 & 0 \\ -\vartheta ct/Ec & -\vartheta ct/Ec & 1/Ec & 0 & 0 & 0 \\ 0 & 0 & 0 & 1/Gt & 0 & 0 \\ 0 & 0 & 0 & 0 & 1/Gc & 0 \\ 0 & 0 & 0 & 0 & 0 & 1/Gc \end{bmatrix} \begin{Bmatrix} \sigma_{11} \\ \sigma_{22} \\ \sigma_{33} \\ \sigma_{12} \\ \sigma_{13} \\ \sigma_{23} \end{Bmatrix}$$

Ec (MPa)	Et (MPa)	vct	vta	Gt (MPa)
120	20	0.3	0.2	47



Figure 7: Representation of the circumferential (C), transversal (T) and axial directions (A) within the meniscus structure.

VI) Details on Surrogate Modeling

The RBF approximation $\tilde{f}(\mathbf{x})$ of the response function $f(\mathbf{x})$ at n arbitrary training points can be found as:

$$\tilde{f}(\mathbf{x}) = \sum_{i=1}^n \lambda_i \phi(\|\mathbf{x} - \mathbf{x}_i\|) \quad (1)$$

where \mathbf{x} is the vector of input variables, \mathbf{x}_i is the vector of input variables at the i^{th} sampling point, $\|\mathbf{x} - \mathbf{x}_i\| = \sqrt{(\mathbf{x} - \mathbf{x}_i)^T (\mathbf{x} - \mathbf{x}_i)}$ is the Euclidean norm representing the radial distance r from design point \mathbf{x} to the sampling point \mathbf{x}_i , ϕ is a radially symmetric basis function, and $\lambda_i, i=1, n$ are the unknown interpolation coefficients. Some of the most commonly used RBF formulations are: $\phi(r) = r^2 \log(r)$ (thin-plate spline); $\phi(r) = e^{-\alpha r^2}$, $\alpha > 0$ (Gaussian); $\phi(r) = \sqrt{r^2 + c^2}$ (multiquadric); and $\phi(r) = 1/\sqrt{r^2 + c^2}$ (inverse multiquadric). Subject to the normalization of r values to the range of (0, 1), the tunings

parameter c lies within $]0, 1]$.

The unknown coefficients in Eq. (1) are found by minimizing the sum of square errors of response approximation at all n training points as expressed by the following:

$$R = \sum_{j=1}^n \left[f(\mathbf{x}_j) - \sum_{i=1}^n \lambda_i \phi(\|\mathbf{x}_j - \mathbf{x}_i\|) \right]^2 \quad (2)$$

Expanding Eq. (S1) leads to a solution for the coefficient vector λ given by

$$\{\lambda\} = [A]^{-1} \{f\} \quad (3)$$

where $[A] = [\phi(\|\mathbf{x}_j - \mathbf{x}_i\|)]$; $j = 1:n$; $i = 1:n$, $\{\lambda\} = \{\lambda_1, \lambda_2, \dots, \lambda_n\}^T$ and $\{f\} = \{f(\mathbf{x}_1), f(\mathbf{x}_2), \dots, f(\mathbf{x}_n)\}^T$. The error statistics PRESS and $R_{Prediction}^2$ as defined by Eqs. (4) and (5) are used to evaluate the accuracy of constructed surrogate models at the training points.

$$PRESS = \sum_{i=1}^n [f_j - \tilde{f}_{(j)}]^2 \quad (4)$$

$$R_{Prediction}^2 = 1 - \frac{PRESS}{SST} \quad (5)$$

where $\tilde{f}_{(j)}$ is the approximation of the response f_j at the j^{th} training point using the RBF model created by $(n - 1)$ training points that exclude the j^{th} point. SST represents the total sum of squares for responses f_j ; $j = 1:n$. In addition, to evaluate the accuracy of the constructed surrogate models at test points, $RSME$ and R^2 statistics defined by Eqs. (6) and (7) are used.

$$RMSE = \sqrt{\frac{SSE}{m}} \quad (6)$$

$$R^2 = 1 - \frac{SSE}{SST} \quad (7)$$

where m is the number of test points. SSE and SST represent the sum of square errors and the total sum of squares for responses at m test points, respectively.

In this paper, for each desired response of the ACL-R simulations, the best choice of RBF basic function, $\phi(r)$, along with the best tuning parameter c was explored. The objective was to find an optimal combination of RBF basic function and tuning parameter c for which the PRESS (Eq. (4)) was the lowest compare to the other possible combinations. To achieve this objective, the following steps were followed:

Step 1: for each desired response, two surrogate models with multiquadratic and inverse multiquadratic RBF functions were built.

Step 2: for each surrogate model of different RBF functions, the tuning parameter c is changed within $]0, 1]$ with an increment of 0.1 (instead of 0, 0.01 is considered), and their accuracy was assessed using Eq. (S3) for each c (0.01, 0.1, 0.2...0.9, 1).

Step 3: With the identification of the range of c associated with the lowest error, c is changed within that range with an increment of 0.01, and the error is assessed for each of them. A value of c associated with the lowest PRESS (Eq. (4)) is chosen for each surrogate model of different RBF functions.

Step 4: for each response, a surrogate model with the lowest PRESS is selected.

VII) Sensitivity indices

The partial variances are defined by the variance of the output Y (ligament forces) when input parameter X_i (6-surgical design parameters) is fixed to its true value. If the true value is unknown, the expectation of the known range of variation of the input is well used as an accepted alternative (Saltelli et al., 2010), leading to the following equations.

$$V_i = V(E(Y|X_i)) \quad (1)$$

$$V_{ij} = V(E(Y|X_i, X_j)) - V(E(Y|X_i)) \quad (2)$$

where $V()$ and $E()$ are the variance and expectation operators, respectively. For higher-order terms, all terms are linked by:

$$V(Y) = \sum V_i + \sum V_{ij} + \dots + V_{12\dots6} \quad (3)$$

Dividing both sides of the equation by $V(Y)$, we obtain the main equation used to figure out the sensitivity indices:

$$\sum_i S_i + \sum_i \sum_{j>i} S_{ij} + \dots + S_{12\dots6} = 1 \quad (4)$$

VIII) Joint Kinematics and contact behavior

Most of the surgical designs (79 %) resulted in medial contact forces within the range of healthy model prediction ($540 \text{ N} \pm 50\text{N}$). However, 21% of the designs that favor an increase in the medial force characterized by an additional anterior location (~ 85% vertically) and higher graft fixation angle (~ 35 degrees) and femoral tunnel orientations that are ranging from 59/39 to 72/55 degrees in the coronal and sagittal plane, respectively. A higher range of fixation angle (31 to 39 degrees) and graft

1
2
3 tensioning force (85 to 116 N) were observed to have the tendency to shift the compartmental load
4 distribution meaningfully from the lateral side to the medial side. Six out of 48 models augmented the
5 lateral joint displacement by nearly 10%. These models were characterized by a high fixation angle
6 and low graft pretension. However, the augmentation of the graft pretension and the tunnel's posterior
7 location led to a posterior displacement of the knee joint.
8
9
10
11

12
13 Graft tensioning force and fixation angle accounted for the major portion of the variance in the
14 joint total contact force (56%). The combined and separate changes in the graft tensioning and fixation
15 angle were mainly controlling the sensitivity of the computed maximum contact stress (48%). Tunnel
16 placement followed by the graft fixation angle were responsible for most of the observed variability
17 of the kinematics of the joint (46%).
18
19
20
21

22 IX) Reference

- 23
24 Adouni, M., Dhaher, Y.Y., 2016. A multi-scale elasto-plastic model of articular cartilage. *J Biomech*
25 49, 2891-2898.
26
27
28 Adouni, M., Faisal, T.R., Gaith, M., Dhaher, Y.Y., 2019. A multiscale synthesis: characterizing acute
29 cartilage failure under an aggregate tibiofemoral joint loading. *Biomech Model Mechanobiol*.
30
31
32 Arnold, M., Netter, H., 1998. Approximation of Contact Geometry in the Dynamical Simulation of
33 Wheel-Rail Systems. *Mathematical and Computer Modeling of Dynamical Systems* 4, 162-184.
34
35
36 Asaro, R.J., Rice, J., 1977. Strain localization in ductile single crystals. *Journal of the Mechanics and*
37 *Physics of Solids* 25, 309-338.
38
39
40 Bernard, M., Hertel, P., Hornung, H., Cierpinski, T., 1997. Femoral insertion of the ACL. Radiographic
41 quadrant method. *Am J Knee Surg* 10, 14-21; discussion 21-12.
42
43
44 Bi, X., Yang, X., Bostrom, M.P., Camacho, N.P., 2006. Fourier transform infrared imaging
45 spectroscopy investigations in the pathogenesis and repair of cartilage. *Biochim Biophys Acta*
46 1758, 934-941.
47
48
49 Buehler, M.J., 2006. Nature designs tough collagen: explaining the nanostructure of collagen fibrils.
50 *Proceedings of the National Academy of Sciences* 103, 12285-12290.
51
52
53 Buehler, M.J., 2008. Nanomechanics of collagen fibrils under varying cross-link densities: atomistic
54 and continuum studies. *Journal of the mechanical behavior of biomedical materials* 1, 59-67.
55
56
57
58
59
60

- 1
2
3 Dhaher, Kwon, T.H., Barry, M., 2010. The effect of connective tissue material uncertainties on knee
4 joint mechanics under isolated loading conditions. *J Biomech* 43, 3118-3125.
5
6
7 Dhaher, Y., Sun, Q., 2006. Three-dimensional Hyperelastic Model of the Human Knee: A Parametric
8 Sensitivity Study. In: 7th World Congress on Computational Mechanics,
9
10
11 Dhaher, Y.Y., Kahn, L.E., 2002. The effect of vastus medialis forces on patello-femoral contact: a
12 model-based study. *Journal of Biomechanical Engineering* 124, 758-767.
13
14
15 Donahue, T.L., Hull, M.L., Rashid, M.M., Jacobs, C.R., 2002. A finite element model of the human
16 knee joint for the study of tibio-femoral contact. *J Biomech Eng* 124, 273-280.
17
18
19 Faisal, T.R., Adouni, M., Dhaher, Y.Y., 2019. The effect of fibrillar degradation on the mechanics of
20 articular cartilage: a computational model. *Biomechanics and modeling in mechanobiology*, 1-
21 19.
22
23
24 Fithian, D.C., Kelly, M.A., Mow, V.C., 1990. Material properties and structure-function relationships
25 in the menisci. *Clinical Orthopaedics and Related Research*, 19-31.
26
27
28 Lee, E.H., 1969. Elastic-plastic deformation at finite strains. *Journal of Applied Mechanics* 36, 1-6.
29
30
31 Limbert, G., Middleton, J., 2004. A transversely isotropic viscohyperelastic material - Application to
32 the modeling of biological soft connective tissues. *International Journal of Solids and Structures*
33 41, 4237-4260.
34
35
36 Nicholas, S.J., 2004. A Prospectively Randomized Double-Blind Study on the Effect of Initial Graft
37 Tension on Knee Stability After Anterior Cruciate Ligament Reconstruction. *American Journal*
38 *of Sports Medicine* 32, 1881-1886.
39
40
41 Piefer, J.W., Pflugner, T.R., Hwang, M.D., Lubowitz, J.H., 2012. Anterior Cruciate Ligament Femoral
42 Footprint Anatomy: Systematic Review of the 21st Century Literature. *Arthroscopy: The*
43 *Journal of Arthroscopic & Related Surgery* 28, 872-881.
44
45
46 Proctor, C.S., Schmidt, M.B., Whipple, R.R., Kelly, M.A., Mow, V.C., 1989. Material properties of the
47 normal medial bovine meniscus. *J Orthop Res* 7, 771-782.
48
49
50 Saltelli, A., Annoni, P., Azzini, I., Campolongo, F., Ratto, M., Tarantola, S., 2010. Variance based
51 sensitivity analysis of model output. Design and estimator for the total sensitivity index.
52 *Computer Physics Communications* 181, 259-270.
53
54
55 Schroeder, M.J., 2010. A Computational Framework to Evaluate the Efficacy of Anterior Cruciate
56 Ligament Reconstruction Procedures. *Biomedical Engineering*. Evanston, illinois, Northwestern
57 university.
58
59
60

- 1
2
3 Schroeder, M.J., 2014. A Multi-Domain Synthesis of Neuromechanical Adaptations Post Anterior
4 Cruciate Ligament Reconstructive Surgery. *Biomedical Engineering*. Evanston, illinois,
5 Northwestern university.
6
7
8 Takeda, Y., Iwame, T., Takasago, T., Kondo, K., Goto, T., Fujii, K., Naruse, A., 2013. Comparison of
9 Tunnel Orientation Between Transtibial and Anteromedial Portal Techniques for Anatomic
10 Double-Bundle Anterior Cruciate Ligament Reconstruction Using 3-Dimensional Computed
11 Tomography. *Arthroscopy: The Journal of Arthroscopic & Related Surgery* 29, 195-204.
12
13
14 Tang, H., Buehler, M.J., Moran, B., 2009a. A constitutive model of soft tissue: from nanoscale collagen
15 to tissue continuum. *Annals of biomedical engineering* 37, 1117-1130.
16
17
18 Tang, H., Buehler, M.J., Moran, B., 2009b. A constitutive model of soft tissue: from nanoscale collagen
19 to tissue continuum. *Ann Biomed Eng* 37, 1117-1130.
20
21
22 Tang, Y., Ballarini, R., Buehler, M.J., Eppell, S.J., 2010. Deformation micromechanisms of collagen
23 fibrils under uniaxial tension. *Journal of The Royal Society Interface* 7, 839-850.
24
25
26 Tissakht, M., Ahmed, A., 1995. Tensile stress-strain characteristics of the human meniscal material.
27 *Journal of Biomechanics* 28, 411-422.
28
29
30 van Kampen, A., 1998. The effect of different graft tensioning in anterior cruciate ligament
31 reconstruction: A prospective randomized study. *Arthroscopy: The Journal of Arthroscopic &
32 Related Surgery* 14, 845-850.
33
34
35 Weiss, J.A., Maker, B.N., Schauer, D.A., 1995. Treatment of initial stress in hyperelastic finite element
36 models of soft tissues. In: *Proceedings of the 1995 Bioengineering Conference*, ASME,
37
38
39 Yasuda, K., Tsujino, J., Tanabe, Y., Kaneda, K., 1997. Effects of Initial Graft Tension on Clinical
40 Outcome After Anterior Cruciate Ligament Reconstruction: Autogenous Doubled Hamstring
41 Tendons Connected in Series with Polyester Tapes. *The American Journal of Sports Medicine*
42 25, 99-106.
43
44
45 Yoshiya, S., Kurosaka, M., Ouchi, K., Kuroda, R., Mizuno, K., 2002. Graft Tension and Knee Stability
46 After Anterior Cruciate Ligament Reconstruction. *Clinical Orthopaedics and Related Research*
47 394, 154-160.
48
49
50
51
52
53
54
55
56
57
58
59
60